JOURNAL OF MATERIALS SCIENCE 27 (1992) 2501–2514

Flow visualization glass–ceramic: preliminary experimental and modelling results

J. PLAWSKY
Department of Chemical Engineering, Rensselaer Polytechnic Institute, Troy, NY 12180, USA

A glass–ceramic material was developed to act as a flow visualization material. Preliminary experiments indicate that aperiodic, thermally induced, convective flows can be sustained at normal processing conditions. These flows and the stress and temperature gradients induced are most likely responsible for the anomalous behaviour seen in these materials and the difficulties encountered in their development and in their production on industrial and experimental scales. A simple model describing the dynamics of variable-viscosity fluids was developed and was shown to be in qualitative agreement with more sophisticated models as well as with experimental results. The model was shown to simulate the dependence of the critical Rayleigh number for the onset of convection on the viscous properties of the fluid at low ΔT, and also to simulate quenching behaviour when the temperature differences were high.

Nomenclature

C_p	Heat capacity
D, E, F	Expansion coefficients
H	Height of the roll cell
Pr	Prandtl number
R_a	Rayleigh number
R_c	Critical Rayleigh number for the onset of convection in a constant-viscosity fluid
S	Dimensionless stream function
T	Temperature
T_m	Mean temperature
T_0	Bottom surface temperature
T_r	Reference temperature
a	Aspect ratio of cell
g	Acceleration due to gravity
k	Thermal conductivity
k_1	Function related to $\partial^2\nu/\partial T^2$
k_2	Function related to $\partial^4\nu/\partial T^4$
r	Rayleigh number ratio R_a/R_c
t	Time
w	Dimensionless vertical coordinate
w_m	Mean cell height
x	Horizontal coordinate
y	Dimensionless horizontal coordinate
z	Vertical coordinate
α, β	Constants
β_t	Thermal expansion coefficient
γ	Constant in viscosity function
ΔT	Temperature difference between top and bottom surfaces
μ_i	Viscosity coefficients
ν	Kinematic viscosity
ν_m	Mean kinematic viscosity
$\mathbf{\nu}$	Dimensionless kinematic viscosity
κ	Thermal diffusivity
θ	Non-linear temperature function
ϕ	Dimensionless non-linear temperature function
σ_o	$\dfrac{2(a^2-1)\Delta T^2 k_1}{\pi^2(1+a^2)^2}$
ψ	Stream function
τ	Dimensionless time
λ	Eigenvalues

1. Introduction

Glasses sensitive to ultraviolet light have been known for centuries. Examples of this "solarization" phenomenon are common and can be found in the purple window-panes of many homes in the USA dating from the colonial period. Sensitivity to sunlight was generally thought to be a nuisance phenomenon and over the centuries, much work has been devoted toward eliminating it. In the 1940s, the process was brought under control and commercial photosensitive glasses and photosensitive glass–ceramics were first developed at Corning Inc. The unique properties of these glasses include reversible fading and darkening upon exposure to ultraviolet light, full colour pattern reproduction (similar to photographic film), and precise photochemical machining of intricate patterns (similar to the patterning of single-crystal silicon). This combination of unique features has resulted in a wide variety of applications for these materials including: microlens arrays for auto-focus cameras, fluidic logic devices, integrated-circuit chip carriers, and polarizing and non-linear optical materials.

The basic process by which most photosensitive glasses and photosensitive glass–ceramics operate follows the much-simplified reaction scheme below [1]:

$$Ag_g^+ + Ce_g^{3+} \xrightarrow[300\text{ nm}]{h\nu} Ag_g^0 + Ce_g^{4+}$$

(metallic silver formation)

$$nAg_g^0 \xrightarrow[\sim 450\,^\circ C]{\text{heat}} (Ag_p^0)_g$$

(metallic silver agglomeration)

0022–2461

$$(Ag_p^0)_g + xR \xrightarrow[\sim 500\,^\circ C]{\text{heat}} C\pi$$

(crystal phase development)

$$C\pi \xrightarrow[\sim 500\,^\circ C]{\text{heat}} C'\pi$$

(silver deposition on to crystals)

Exposure to ultraviolet light induces cerium to eject an electron which results in silver ion reduction to the metal. A subsequent heat treatment causes agglomeration of silver metal atoms and these clusters catalyse the nucleation of a crystal phase. The heat treatment usually involves two temperatures: one to form the crystal nuclei and another to initiate their growth.

The work presented here was motivated by problems seen in the reliable development and manufacture of photosensitive glasses. These materials are notoriously difficult to produce and reproduce on a daily basis as their photosensitive properties change in a seemingly random manner. On an experimental scale, verification of the results of a single successful experiment may require hundreds of repeated trials. Success is somewhat better on a plant scale since process variables are under tighter control. Catastrophic failures (total loss of sensitivity) still occur and without apparent cause. Even when a plant has a successful run or set of runs, the properties of the glass are found to change from run to run and may even vary as a function of time during a single run. To compensate for this uncertainty manufacturers widen specification ranges and reject an unacceptably high amount of potential product.

The premise of this work is that a lack of knowledge and control over the convective flow and temperature fields present in the glass during processing is the cause of most of the difficulties seen in the development and production of these materials. The glasses must be melted at temperatures in excess of 1450 °C to convert cerium, originally in a 4+ oxidation state, to its 3+ oxidation state (this state is favoured at high temperatures in glass). Without this conversion the glass would not be photosensitive in a useful sense. At the melt temperature, the glass viscosity may be as low as 100 poise and due to the large amount of alkali content, the electrical and hence the thermal conductivity of the material may also be quite large. In a normal experimental processing situation where the glass is poured into a mould or as a slab on a bench, the large differences in temperature between the surfaces will result in strong convective motion and high thermal and stress gradients. To insure photosensitivity, cerium must be held in its 3+ oxidation state as the glass cools. This requires precise control over the oxidation state of the glass. Since the activity coefficients of the components vary strongly with temperature, control of the oxidation state is difficult and may be nearly impossible in the presence of thermally induced convection. Clearly studies of natural convection in glass systems will be important if the processes used to produce these materials are to be brought under control.

The remainder of this paper will discuss a new glass–ceramic material developed to act as a flow visualization tool, and a highly simplified model is developed to assess the types of flow possible in glass systems.

2. Development of a flow visualization glass–ceramic

Flows in glasses are related to the general case of flow in a fluid with variable viscosity. Rayleigh–Benard convection in these types of fluid has been the subject of much experimental [2–8] and theoretical interest [9–33] for those working in fluid mechanics, and has spawned a whole field of geology concerned with numerical simulations of mantle convection [34–43]. Though similarities exist between the work just mentioned and glass flows, some important differences remain. Experimental studies of Rayleigh–Benard convection in variable-viscosity fluids are conducted using fluids easily manipulated at room temperature: paraffin, corn syrup, glycerine, etc. [2–8, 44–46]. These fluids may represent the viscosity–temperature behaviour of glasses to some degree, but other equally important physical properties such as density, thermal expansion coefficient and thermal conductivity are nowhere near representative. Therefore experiments based on these materials cannot be extrapolated to explaining glass flow dynamics. Theoretical investigations into these flows, even mantle flows, are also not representative of glass processing conditions. The majority of theoretical treatments assume the Prandtl number to be infinite and so neglect heat conduction entirely. Molten photosensitive glasses have high thermal conductivities coupled with low viscosities, and so an infinite Prandtl number assumption is clearly not valid. Moreover, radiation is one of the dominant forms of heat transfer in glass processing and is of no consequence in the thermal convection of room-temperature fluids. Though glasses are transparent to most thermal radiation, the presence of radiative heat transfer results in severe non-linear temperature gradients in the glass and contributes to non-uniformities in the flow field. Clearly, new experimental and theoretical models are needed to accurately investigate glass flows.

Fig. 1 shows the free surface of a glass–ceramic developed for use as a flow visualization tool. The glass is a lithium–borosilicate composition based on a combination of well-known photosensitive sodium borosilicate compositions and popular lithium aluminosilicate, photosensitive, glass–ceramic compositions. The glass contains the photosensitizing dopant materials Ag^+, Au^{3+} and Ce^{3+} which act as nucleating agents for the crystallization of the glass–ceramic. Upon being poured into a mould and allowed to cool, thermal convection begins and the cellular structure of the flow can be observed due to radiative heat loss. As the glass cools further it phase-separates and mass transfer occurs as the components of the glass (SiO_2, B_2O_3, Li_2O, Al_2O_3, Sb_2O_3, Ag_2O, SnO_2, Au and CeO_2) are redistributed among the various phases (crystal, silica-rich and boron-rich). The boron-rich phase becomes the dispersed phase and produces the stream-lines shown in the figure. It

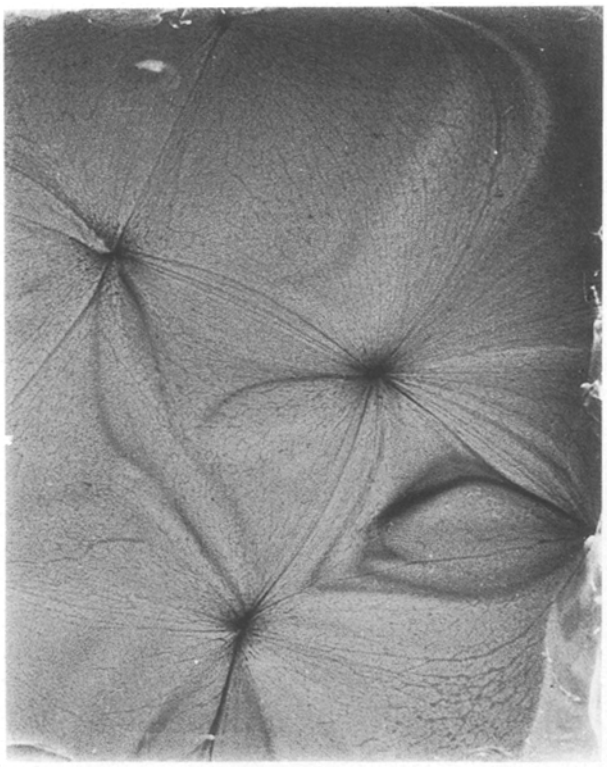

Figure 1 Top surface view of a photosensitive glass slab showing interfacial instability at the glass–air interface and the near-square-cell convective pattern.

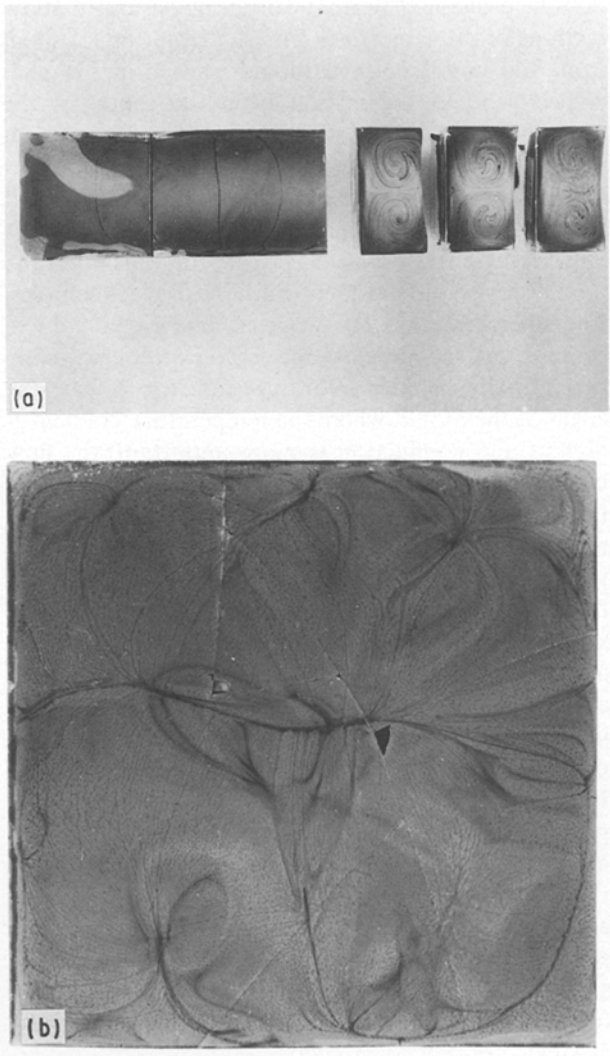

Figure 2 (a) Roll-cell convective patterns: internal and surface views. (b) Spoke-shaped surface convective patterns (prominent at image corners).

cannot crystallize and so remains a glass. The oxidation state of the glass is such that the silver becomes reduced during the cooling process, giving the boron phase a dark brown colour and the opaque, silica-rich, glass–ceramic phase a yellow colour. The contrast between the phases provides for easy viewing of the stream-lines.

The surface convective geometries that are possible in Rayleigh–Benard convection span a range from roll cells to hexagons, squares, triangles, spokes, etc. Using a corn syrup, White [8] has catalogued these flows and the Rayleigh number ranges over which they either first appear spontaneously, or can be induced to appear. In working with a glass, it is difficult to accurately control lower and upper surface temperatures and so a repetition of White's experiments would be nearly impossible. What can be controlled is the geometry of the flow situation and the initial temperature of the glass. Fig. 2 shows surface convective geometries from a series of preliminary experiments where mould geometry was controlled. The mould geometries investigated are given in Table I. The glass–ceramic developed in this work was used and the initial glass temperature was set at 1500 °C. One can see that by varying the geometry, roll cell (Fig. 2a), square cell (Fig. 1), or spoke-shaped patterns (Fig. 2b) can be produced spontaneously. By holding the processing temperature and the glass composition constant, corresponding to holding the initial Rayleigh number (based on mould depth) constant, the whole range of flow behaviour can be investigated simply by changing the geometry or aspect ratio of the mould. In these simple experiments, the surface temperatures were not accurately monitored, but initial Rayleigh numbers were in a range from 10^4 to 10^5.

TABLE I Mould dimensions

Figure	Mould dimensions, $L \times W \times H$	
	(inches)	(mm)
1	$6 \times 4 \times 0.75$	$152 \times 102 \times 19$
2a	$12 \times 2 \times 0.75$	$305 \times 51 \times 19$
2b	$6 \times 6 \times 0.75$	$152 \times 152 \times 19$
3a–c	$6 \times 4 \times 0.75$	$152 \times 102 \times 19$

Of more importance than the surface flows is the nature of the internal flows in these materials. The glass–ceramic has a very steep viscosity–temperature curve so the internal flow field is essentially frozen in place as the glass cools. The glass can then be sectioned to look at internal flows. Fig. 2a shows a pair of roll cells, the stable flow for this elongated geometry. While some fluid mixing is evident in the folding of stream-lines at the centre of the cells, there is little communication throughout the fluid and segregated components have no way of remixing. Changing the geometry slightly to that of Fig. 2b shows that the

flow field changes dramatically. Fig. 3a and b show sections of the same glass represented in Fig. 1, taken from the middle of the mould and from the end, respectively. In the section from the centre of the mould one can see the steady convective flow pattern which occurs in the form of two cells. The mould is twice as wide as that used for the glass of Fig. 2a and the horizontal wavelength of the cells is also twice as large. The vertical wavelengths of the cells span the mould depth and are identical in both glass samples. The interaction of the two cells in Fig. 3a induces some vortex shedding, so one could expect marginally better mixing behaviour for this geometry. Toward the edges of the mould where the temperature gradient is highest and conduction is more important, the flow becomes very complicated and involves the interaction and destruction of many cells. The flow here is reminiscent of flows observed in chaotic mixing of viscous fluids [31] and shows a regime where efficient fluid mixing can occur and where any segregation which may exist in the glass due to insufficient mixing in the melt can be eliminated. These complex flows also have large temperature and stress gradients, making control of the oxidation state difficult. Similar and perhaps more complicated patterns can be seen in Fig. 3c. These flow patterns suggest that aperiodic and possibly chaotic flows can be sustained in these types of glass during typical processing conditions. If so, these flows would be responsible for the difficulties encountered in processing these materials on an experimental and industrial scale. In pursuit of this idea, a simple flow model was developed to investigate the range of flows which might be encountered in these glasses.

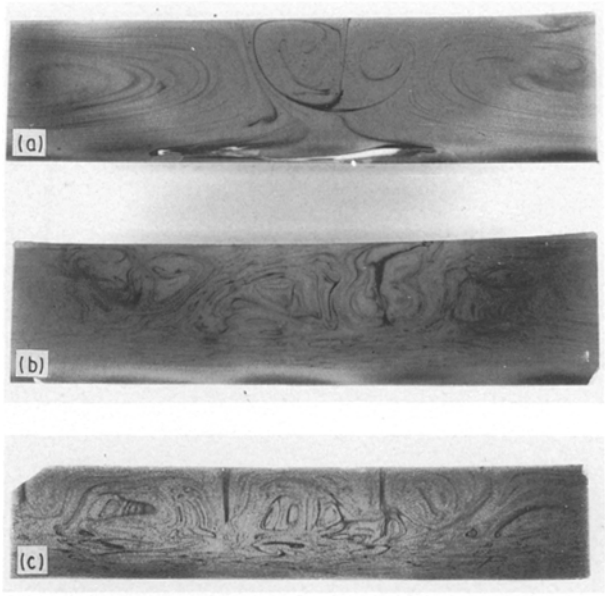

Figure 3 (a) Mid-section slice from Fig. 1 showing the roll-cell pattern. (b) End-section slice from Fig. 1 showing complex geometrical patterns. (c) End section showing complex cellular flow patterns and the effects of increased conductive heat transfer.

3. Model development

The simplest model capable of describing some of the dynamics of the glass system considers only a single two-dimensional cell with free boundaries, and is developed following a simplification procedure first outlined by Saltzman [29] and Lorenz [23]. Many papers have been devoted to the study of the equations they developed for a constant-viscosity fluid and the validity of those equations as a flow model [16]. Lorenz showed that a truncated model of this type conserves the mean kinetic energy and the mean square vorticity of the flow [24]. The model developed here for variable-viscosity fluids also conserves the mean kinetic energy and mean square of the vorticity but cannot conserve the entire statistical distribution of the vorticity, and so will not be able to reproduce experimental results in detail. Still, a model of this type is useful for anticipating the range of dynamic conditions which may appear in the flows, for elucidating the most important features of the flow and for relating those features to the physical system in a way which is easily interpreted and used as a guide by process engineers.

The Boussinesq approximation is assumed to be valid over the temperature range of interest ($\Delta T \leqslant 200\,^{\circ}\mathrm{C}$) and for sodium silicate glasses similar to the composition used here, this appears to be the case [47]. Since the density in the continuity equation is assumed to be nearly constant, the pressure terms in the momentum equation can be removed by forming the stream function, ψ, in a manner similar to Torrence and Turcotte [33].

The temperature field is defined by splitting it into the sum of the average temperature at the base of the system, T_0, a linear function representing the overall temperature gradient due to conduction from the base to the top of the system, $\Delta Tz/H$, and a non-linear term describing the deviations in both the horizontal and vertical directions, θ:

$$T(x, z, t) = T_0 - \frac{\Delta T}{H} z + \theta(x, z, t) \qquad (1)$$

The energy equation becomes a function of the non-linear component of the temperature θ, and the stream function, ψ.

The viscosity μ of the glass is a very strong function of temperature which has been found to obey the following empirical relationship:

$$\mu = \mu(T_r)\exp\left[-\gamma\left(\frac{T_r}{T} - 1\right)\right] \qquad (2)$$

where T_r is a reference temperature for the glass. This form for the viscosity function proved very difficult to manipulate during the construction of this model and did not lend itself to further simplification. Therefore, a five-term polynomial of the form

$$\mu = \mu_0 + \mu_1(T - T_0) + \mu_2(T - T_0)^2 + \mu_3(T - T_0)^3 + \mu_4(T - T_0)^4 + \mu_5(T - T_0)^5 \qquad (3)$$

was used instead. The best definition for the polynomial viscosity function was obtained when the

coefficients of Equation 3 were determined by matching the respective functions (Equations 2 and 3) and their first five derivatives evaluated at the mean temperature of the calculation, T_m.

The stream function, energy, and viscosity equations were made dimensionless by the following transformations:

$$y = \frac{x}{H} \qquad w = \frac{z}{H} \qquad S = \frac{\psi}{k} \tag{4a}$$

$$\tau = \frac{\pi^2(1 + a^2)\kappa t}{H^2} \qquad \phi = \frac{g\beta_t H^3}{\kappa \nu_m} \qquad \nu = \frac{\nu}{\nu_m} \tag{4b}$$

$$\nu_m = \nu_0 - \nu_1(\Delta T w_m) + \nu_2(\Delta T w_m)^2 - \nu_3(\Delta T w_m)^3 + \nu_4(\Delta T w_m)^4 - \nu_5(\Delta T w_m)^5 \tag{4c}$$

where ν_m represents the mean kinematic viscosity of the fluid. Substituting the new variables into the stream function, energy, and viscosity equations yields the following:

Stream function

$$\begin{aligned}
&\pi^2(1 + a^2)\frac{\partial}{\partial \tau}\left(\frac{\partial^2 S}{\partial y^2} + \frac{\partial^2 S}{\partial w^2}\right) - \frac{\partial S}{\partial w} \\
&\times\left(\frac{\partial^3 S}{\partial y^3} + \frac{\partial^3 S}{\partial w^2 \partial y}\right) + \frac{\partial S}{\partial y}\left(\frac{\partial^3 S}{\partial w^3} + \frac{\partial^3 S}{\partial w \partial y^2}\right) \\
&- Pr\frac{\partial \phi}{\partial y} - Pr\nu\left(\frac{\partial^4 S}{\partial y^4} + \frac{\partial^4 S}{\partial w^4} + 2\frac{\partial^4 S}{\partial y^2 \partial w^2}\right) \\
&- 2Pr\frac{\partial \nu}{\partial w}\left(\frac{\partial^3 S}{\partial w^3} + \frac{\partial^3 S}{\partial w \partial y^2}\right) \\
&- 2Pr\frac{\partial \nu}{\partial y}\left(\frac{\partial^3 S}{\partial y^3} - \frac{\partial^3 S}{\partial y \partial w^2}\right) \\
&- 4Pr\frac{\partial^2 \nu}{\partial y \partial w}\left(\frac{\partial^2 S}{\partial y \partial w}\right) + Pr\frac{\partial^2 \nu}{\partial w^2}\left(\frac{\partial^2 S}{\partial y^2} - \frac{\partial^2 S}{\partial w^2}\right) \\
&- Pr\frac{\partial^2 \nu}{\partial y^2}\left(\frac{\partial^2 S}{\partial y^2} - \frac{\partial^2 S}{\partial w^2}\right) = 0
\end{aligned} \tag{5}$$

Energy

$$\pi^2(1 + a^2)\frac{\partial \phi}{\partial \tau} - \left(\frac{\partial S}{\partial w}\right)\frac{\partial \phi}{\partial y} + \left(\frac{\partial S}{\partial y}\right)\frac{\partial \phi}{\partial w} - R_a\frac{\partial S}{\partial y} - \frac{\partial^2 S}{\partial y^2} - \frac{\partial^2 S}{\partial w^2} = 0 \tag{6}$$

Kinematic viscosity

$$\begin{aligned}
\nu = \frac{1}{\nu_m}\Bigg[&\nu_0 + \nu_1\left(\frac{\Delta T}{R_a}\right)(\phi - R_a w) \\
&+ \nu_2\left(\frac{\Delta T}{R_a}\right)^2(\phi - R_a w)^2 \\
&+ \nu_3\left(\frac{\Delta T}{R_a}\right)^3(\phi - R_a w)^3 \\
&+ \nu_4\left(\frac{\Delta T}{R_a}\right)^4(\phi - R_a w)^4 \\
&+ \nu_5\left(\frac{\Delta T}{R_a}\right)^5(\phi - R_a w)^5\Bigg]
\end{aligned} \tag{7}$$

The Prandtl number, Pr, and the Rayleigh number, R_a, are evaluated at the mean temperature of the fluid:

$$Pr = \frac{\nu_m}{\kappa} \qquad R_a = \frac{g\beta_t \Delta T H^3}{\nu_m \kappa} \tag{8}$$

The simplest form of the model considers only the first harmonic of the stream function in the horizontal and vertical directions, the first harmonic of the temperature field in the horizontal direction and the first and second harmonics of the temperature field in the vertical direction.

$$S = \frac{\alpha}{\kappa} F \sin(\pi a y)\sin(\pi w) \tag{9}$$

$$\phi = \frac{r}{\Delta T}\left[D\cos(\pi a y)\sin(\pi w) - \frac{1}{2}E\sin(2\pi w)\right] \tag{10}$$

where

$$\alpha = \frac{\kappa(1 + a^2)}{a} \qquad \beta = \frac{\Delta T}{\pi r} = \frac{\pi^3(1 + a^2)^3 \Delta T}{a^2 R_a} \tag{11}$$

and a represents the aspect ratio for the cellular motion in the horizontal and vertical directions. The coefficients F, D and E are time-dependent quantities only. The above representations are substituted into the stream, energy and viscosity functions. These equations are reduced, where possible, into contributions from $\sin(\pi a y)\sin(\pi w)$, $\cos(\pi a y)\sin(\pi w)$, and $\sin(2\pi w)$. Like terms are grouped together to generate the following three equations describing the dynamic behaviour of the coefficients F, D and E.

$$\begin{aligned}
\frac{\partial F}{\partial \tau} = &\left(\frac{Pr}{\beta}\right)D - Pr\left(1 - \frac{2(a^2 - 1)\Delta T^2 k_1}{\pi^2(1 + a^2)^2}\right)F \\
&- Prk_1\left(1 - \frac{4a^2(3 - a^2)}{(1 + a^2)^2} - \frac{12(a^2 - 1)\Delta T^2 k_2}{\pi^2(1 + a^2)^2 k_1}\right)FD^2 \\
&- Prk_1\left(\frac{1}{4} + \frac{8}{(1 + a^2)^2} - \frac{3(a^2 - 1)\Delta T^2 k_2}{\pi^2(1 + a^2)^2 k_1}\right)FE^2 \\
&- Prk_2\left(1 - \frac{8(7a^2 - 1)}{(1 + a^2)^2}\right)FD^4 \\
&- Prk_2\left(\frac{1}{16} - \frac{2(a^2 - 3)}{(1 + a^2)^2}\right)FE^4 \\
&- \frac{3}{2}Prk_2\left(1 + \frac{4a^2(a^2 + 17)}{(1 + a^2)^2}\right)FD^2E^2 \\
&+ 2Prk_1\Delta T\left(\frac{(3 + a^2)}{\pi(1 + a^2)^2}\right)FE \\
&+ Prk_2\Delta T\left(\frac{(5 - a^2)}{\pi(1 + a^2)^2}\right)FE^3 \\
&+ 12Prk_2\Delta T\left(\frac{(13a^2 - 1)}{\pi(1 + a^2)^2}\right)FD^2E
\end{aligned} \tag{12}$$

$$\frac{\partial D}{\partial \tau} = -FE - D + \beta r F \tag{13}$$

$$\frac{\partial E}{\partial \tau} = FD - \frac{4}{1+a^2}E \tag{14}$$

The constants k_1 and k_2 are proportional to the derivatives of the viscosity with respect to the temperature and are given by

$$k_1 = \frac{1}{\nu_m}[\nu_2 - 3\nu_3(\Delta T w_m) + 6\nu_4(\Delta T w_m)^2 - 10\nu_5(\Delta T w_m)^3]$$

$$\propto \left.\frac{\partial^2 \nu}{\partial T^2}\right|_{T_m} \tag{15}$$

$$k_2 = \frac{1}{\nu_m}[\nu_4 - 5\nu_5(\Delta T w_m)] \propto \left.\frac{\partial^4 \nu}{\partial T^4}\right|_{T_m} \tag{16}$$

Since both ϕ and S are even functions of w, no matter how severe the truncation in the series solution [16], the presence of the second-order and fourth-order derivatives in the representation of the viscosity is a fundamental feature of the solution.

F is a measure of the strength of the flow in the cell. The flow is clockwise if F is positive and counterclockwise when F is negative. D represents a measure of the horizontal temperature gradient. It follows F such that when F is positive, D is positive, indicating hot fluid rising from the left-hand side of the cell and cold fluid descending on the right-hand side. When F and D are negative, cold fluid is descending on the left-hand side. Large values of D represent large temperature gradients near the edges of the cell or thin boundary layers and relatively uniform temperatures in the centre of the cell. E is a measure of the temperature gradient in the vertical direction. Large values of E indicate that the boundary layers at the upper and lower surfaces are thin and that the temperature is fairly uniform in the centre. Equations 12–14 reduce to the familiar Lorenz equations when the assumption of constant viscosity is applied. In general, for fluids whose viscosity decreases with increasing temperature, the terms in Equation 12 with odd powers of E represent forcing functions (same sign as F) whereas the terms with even powers of E represent damping functions (opposite in sign to F).

In the next two sections preliminary results from this model will be discussed. They are presented to show that the highly simplified model displays realistic behaviour at both large and small values of the temperature difference, ΔT. A linear stability analysis is used to check predictions at small ΔT and numerical calculations to check one possible large ΔT prediction.

3.1. Onset of convection

One of the most important predictions of the models used to describe the fluid flow with temperature-dependent viscosity is that the critical Rayleigh number for the onset of convection should increase as the viscosity range spanned by the fluid increases. Once the viscosity range grows to nearly a thousand-fold, the critical Rayleigh number levels off and begins to decrease (Fig. 4). This prediction and its experimental confirmation were the subject of much controversy in the 1970s when various conflicting predictions concerning the behaviour of the critical Rayleigh number were made. Each conflicting prediction was then confirmed experimentally [2, 4, 7]. Recently, reliable data [8] have shown that the trend mentioned above is correct.

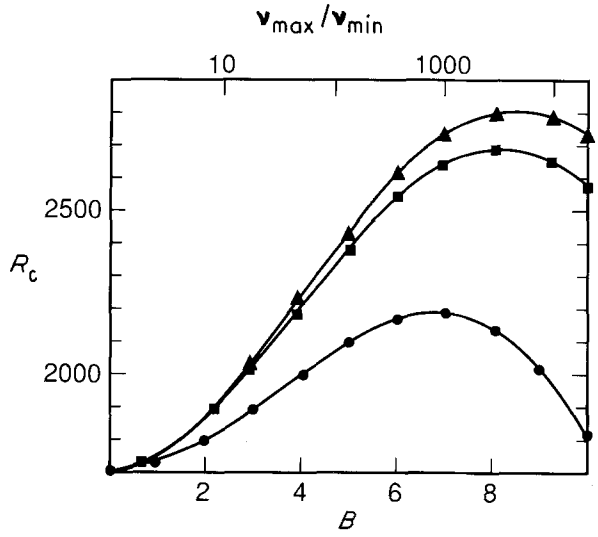

Figure 4 A plot of the critical Rayleigh number, R_c, versus $B = \ln(\nu_{max}/\nu_{min})$ [8]: (●) experimental viscosity fluid, (■) golden syrup, (▲) golden syrup–variable k.

The stability of a solution $F = D = E = 0$, representing the case of no convection to a small disturbance, is initially governed by the characteristic equation

$$\left(\lambda + \frac{4}{1+a^2}\right)\{\lambda^2 + [Pr(1-\sigma_o) + 1]\lambda + Pr(1 - \sigma_o - r)\} = 0 \tag{17}$$

The solution has three real roots when r, the ratio between the Rayleigh number for the fluid to the critical Rayleigh number for the onset of convection in a constant-viscosity fluid, is greater than zero. Of these three solutions, all are negative when $r < 1 - \sigma_o$ indicating that a purely conductive solution is stable. When $r > 1 - \sigma_o$ there is one real positive root so the conductive solution is unstable. The onset of convection must occur when

$$r_c = 1 - \sigma_o = 1 - \frac{2(a^2-1)\Delta T^2 k_1}{\pi^2(1+a^2)^2} \tag{18}$$

For a constant-viscosity fluid ($k_1 = 0$), the critical Rayleigh number ratio for the onset of convection, r_c, is equal to unity and this agrees with Rayleigh's original analysis. The present model predicts a variation in critical Rayleigh number ratio as a function of the fluid properties, the cell geometry, and of the temperature difference between the bounding planes. The term σ_o arises from the $\partial \mathbf{v}/\partial w$ and $\partial^2 \mathbf{v}/\partial w^2$ terms in the stream-function Equation 5.

The critical Rayleigh number ratio is highly dependent upon the temperature difference between the upper and lower surfaces. There is an explicit quadratic dependence on ΔT in the σ_o term and k_1 is also dependent on the temperature difference and on the definition of the mean temperature. The origin of the temperature dependence is clear. The term $2k_1$ is the second derivative of the viscosity with respect to

the temperature. The term $2\Delta T^2 k_1$ represents the viscosity range spanned by the fluid between the upper and lower boundaries. Previous models for temperature-dependent viscous fluids have presented figures showing the dependence of the critical Rayleigh number on the ratio of the viscosities at the two temperature extremes [8, 11]. From this model, we see that to a first approximation it is not just the viscosity range which is important or the fact that the viscosity changes with temperature, but it is the curvature of the viscosity–temperature relationship which is primarily responsible for the observed effects.

Glasses and most other fluids display an exponential viscosity–temperature behaviour where the viscosity decreases with increasing temperature. In such fluids, the curvature of the viscosity–temperature relationship is positive. Therefore, for aspect ratios less than unity, corresponding to most experimental conditions, this simple model predicts that the critical Rayleigh number should increase with increasing temperature difference between the hot and cold surfaces. A graph of the critical Rayleigh number ratio, r_c, as a function of the log of the maximum viscosity ratio, $\ln(\nu_{max}/\nu_{min})$, for a glass is shown in Fig. 5. The physical parameters used in the calculation are given in Table II and were chosen to represent the photosensitive glass of Figs 1–3 as closely as possible. Four curves are given representing two different definitions of the mean temperature and two aspect ratios. The two curves at the upper and lower extremes of the figure were based on a mean temperature defined by weighting the linear temperature profile by the viscosity

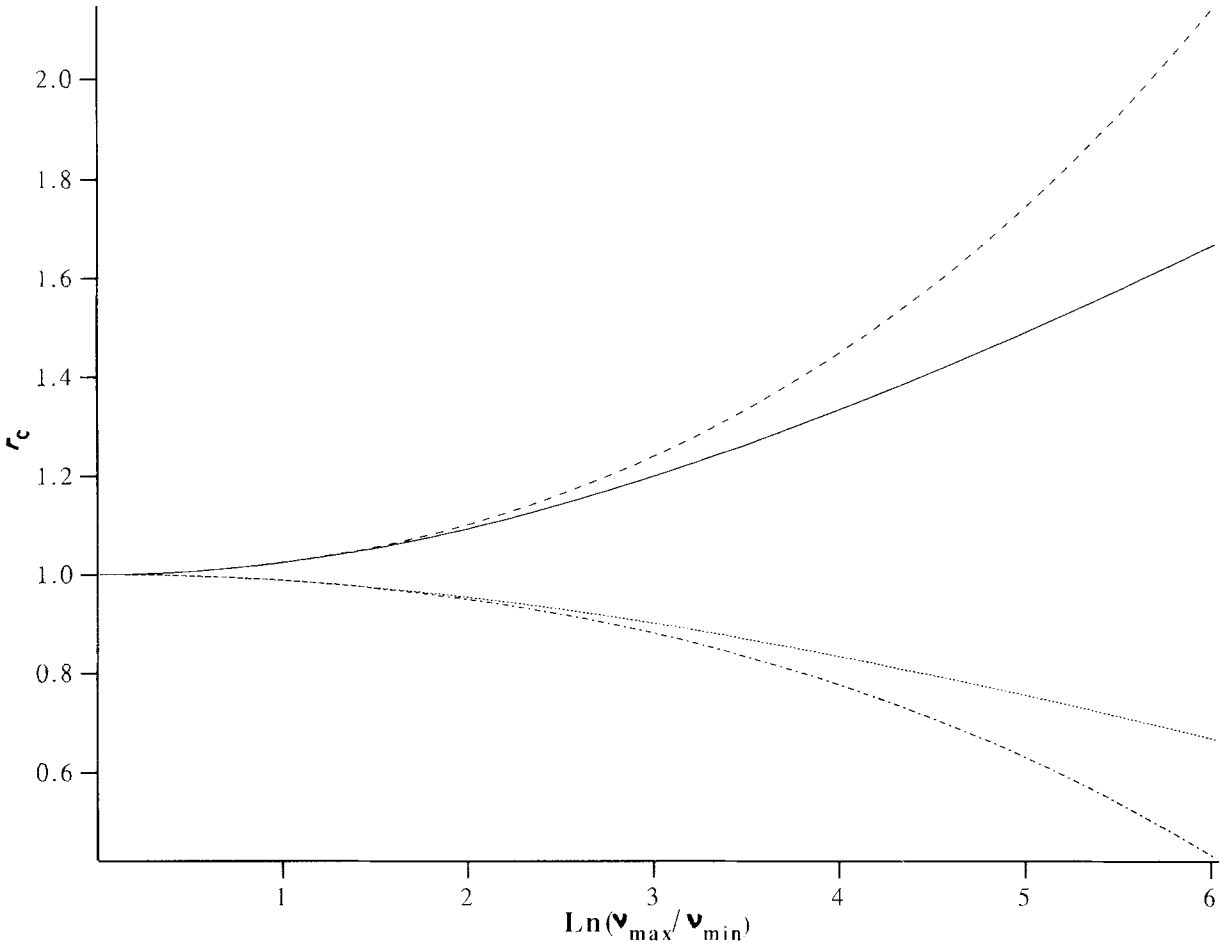

Figure 5 Critical Rayleigh number ratio, $r_c = R_a/R_c$, at the onset of steady convection. Fluid properties are evaluated at the mean temperature defined by Equations 19 and 20. (——) $a^2 = 0.5$, T_m weighted by $1/\mu$; (· · ·) $a^2 = 2.0$, T_m weighted by $1/\mu$; (– – –) $a^2 = 0.5$, T_m weighted by μ; (– · –) $a^2 = 2.0$, T_m weighted by μ.

TABLE II Physical properties of photosensitive glass

Viscosity, μ ($kg\,m^{-1}\,s^{-1}$)	$(1.5 \times 10^5)\exp\{40[(900/T) - 1]\}$
Density, ρ ($kg\,m^{-3}$)	2360
Thermal expansion coefficient, β (K^{-1})	3.7×10^{-3}
Thermal conductivity, k ($W\,m^{-1}\,K^{-1}$)	24.24
Heat capacity, C_p ($kJ\,kg^{-1}\,K^{-1}$)	1000
Box height, H (m)	0.0369
Aspect ratio, a^2	0.25–2.0
Temperature range, ΔT (°C)	0–200

of the fluid at that temperature:

$$T_{mh} = \frac{\int_{T_H}^{T_o} T\exp\{\gamma[(T_r/T) - 1]\}\,dT}{\int_{T_H}^{T_o} \exp\{\gamma[(T_r/T) - 1]\}\,dT} \quad (19)$$

This definition for the mean temperature emphasizes the upper, highly viscous region of the flow. With this definition, the model predicts an exponential increase in the critical Rayleigh number with increasing ΔT. In that sense the trend is in agreement with the calculations and experimental observations of Stengel *et al.* [30] and White [8], who observed what looks like a nearly exponential growth of r_c with increasing viscosity ratio (Fig. 4 for $\ln(\nu_{max}/\nu_{min}) \leqslant 3$). An alternative definition for the mean temperature emphasizes the lower-viscosity sub-layer by weighting the temper-

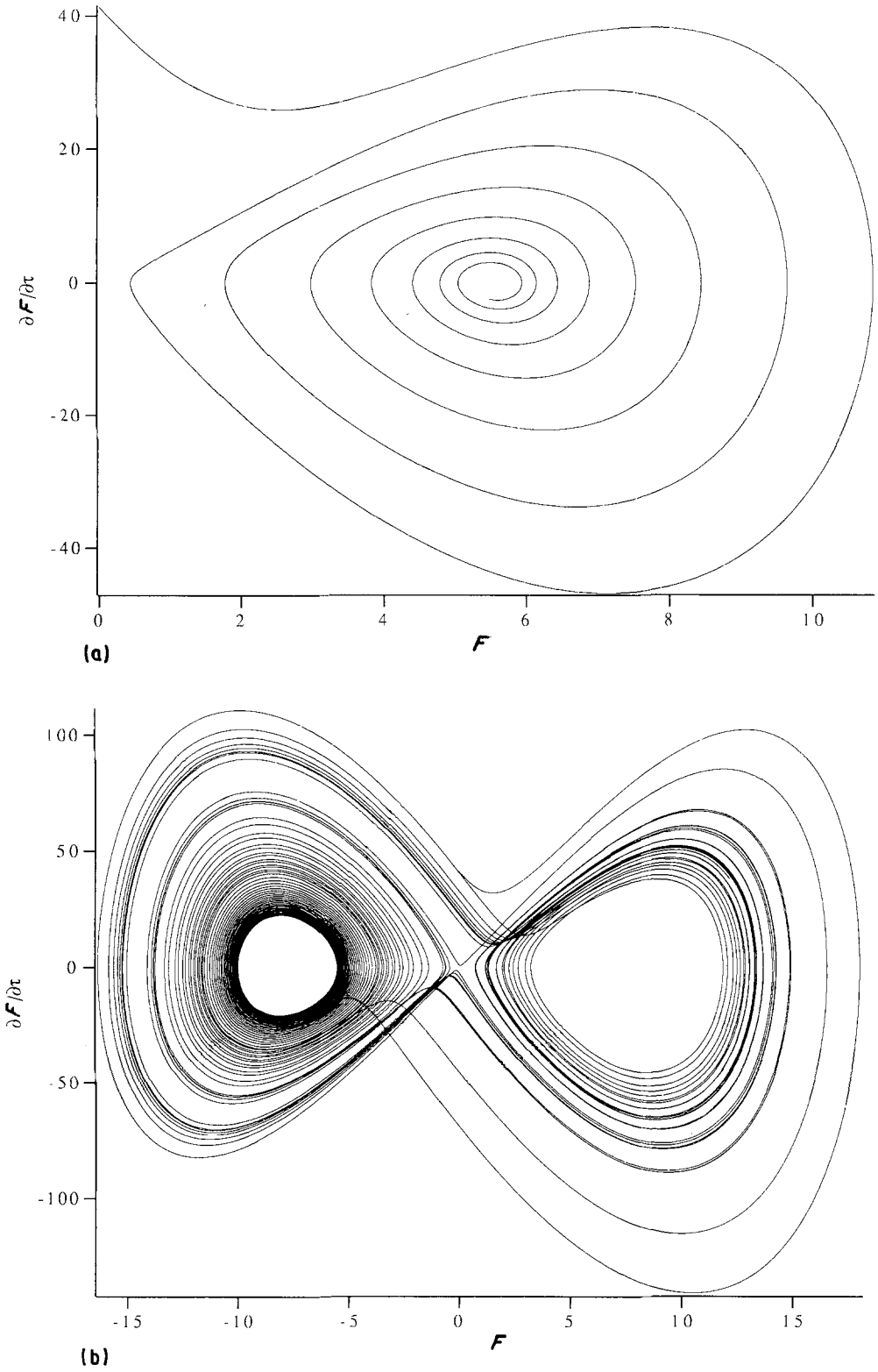

Figure 6 Phase-plane diagrams for the test glass. Fluid properties evaluated at the mean temperature defined by Equation 20. (a) $r = 12.52$, $Pr = 10.52$, $\Delta T = 5\,^{\circ}C$, $a^2 = 0.50$; (b) $r = 23.88$, $Pr = 11.03$, $\Delta T = 10\,^{\circ}C$, $a^2 = 0.50$; (c) $r = 124.80$, $Pr = 19.00$, $\Delta T = 90\,^{\circ}C$, $a^2 = 0.50$; (d) $r = 141.20$, $Pr = 20.53$, $\Delta T = 110\,^{\circ}C$, $a^2 = 0.50$; (e) $r = 157.42$, $Pr = 21.76$, $\Delta T = 130\,^{\circ}C$, $a^2 = 0.50$; (f) $r = 174.06$, $Pr = 22.71$, $\Delta T = 150\,^{\circ}C$, $a^2 = 0.50$; (g) $r = 178.57$, $Pr = 22.91$, $\Delta T = 155.28\,^{\circ}C$, $a^2 = 0.50$; (h) $r = 182.64$, $Pr = 23.08$, $\Delta T = 160\,^{\circ}C$, $a^2 = 0.50$.

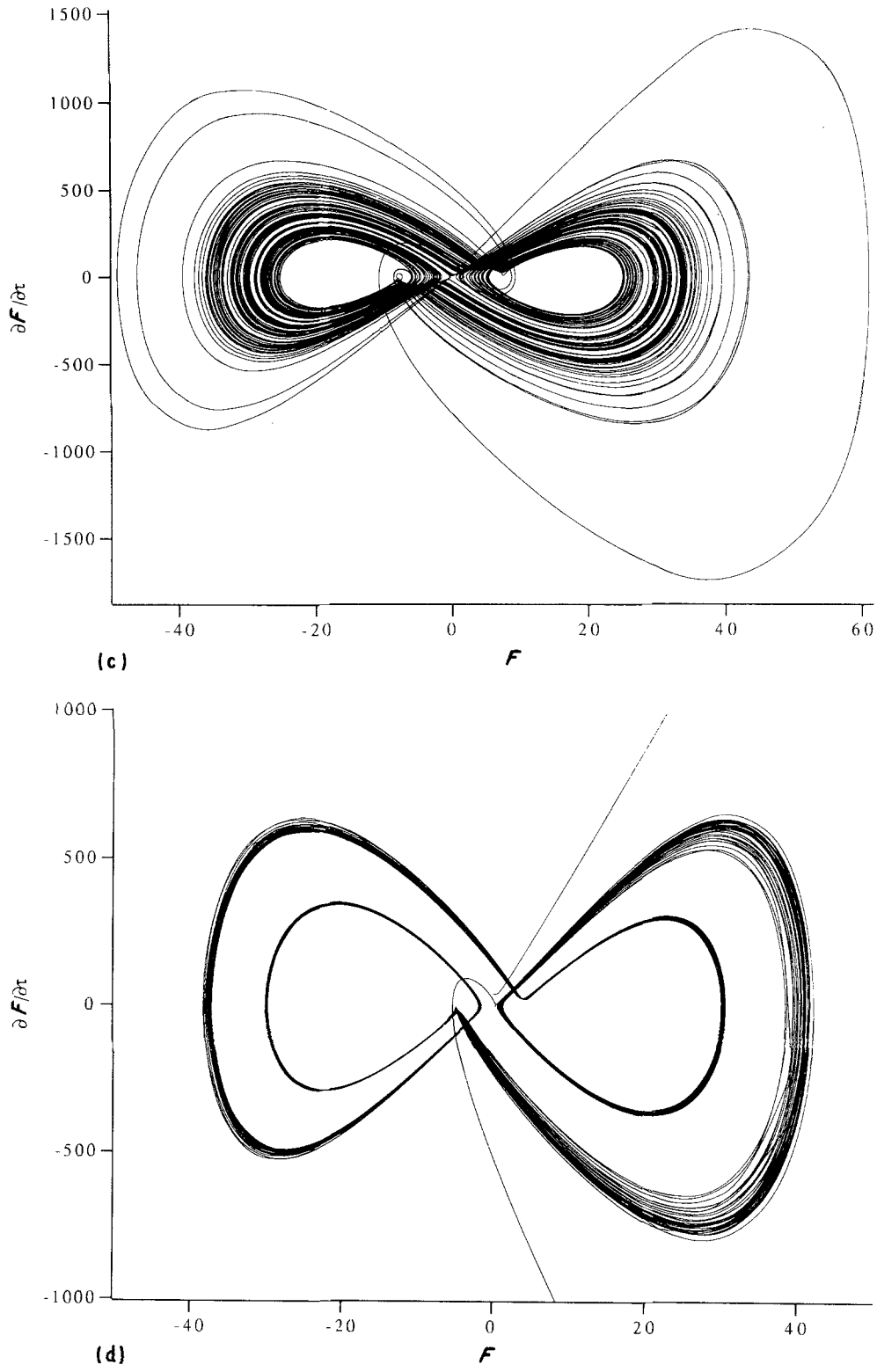

Figure 6 Continued

ature with the inverse of the viscosity according to

$$T_{\mathrm{ml}} = \frac{\int_{T_H}^{T_o} T\exp\{-\gamma[(T_r/T) - 1]\}\,\mathrm{d}T}{\int_{T_H}^{T_o} \exp\{-\gamma[(T_r/T) - 1]\}\,\mathrm{d}T} \qquad (20)$$

The two inner curves of Fig. 5 show that in this case there is an initial region of exponential growth of r_c with ΔT which then levels off as ΔT increases, becoming a region of quadratic growth once the viscosity ratio reaches about 10 or so. The decrease in r_c growth rate with ΔT is in better agreement with the calculations and experiments of Stengel *et al.* and White up to $\ln(\nu_{max}/\nu_{min}) \approx 6$, but this truncated model cannot predict the subsequent levelling off and decrease of r_c at extreme viscosity ratios. At these points the single-cell solution assumed here may be intrinsically unstable and higher-order harmonic terms are necessary to describe the solution.

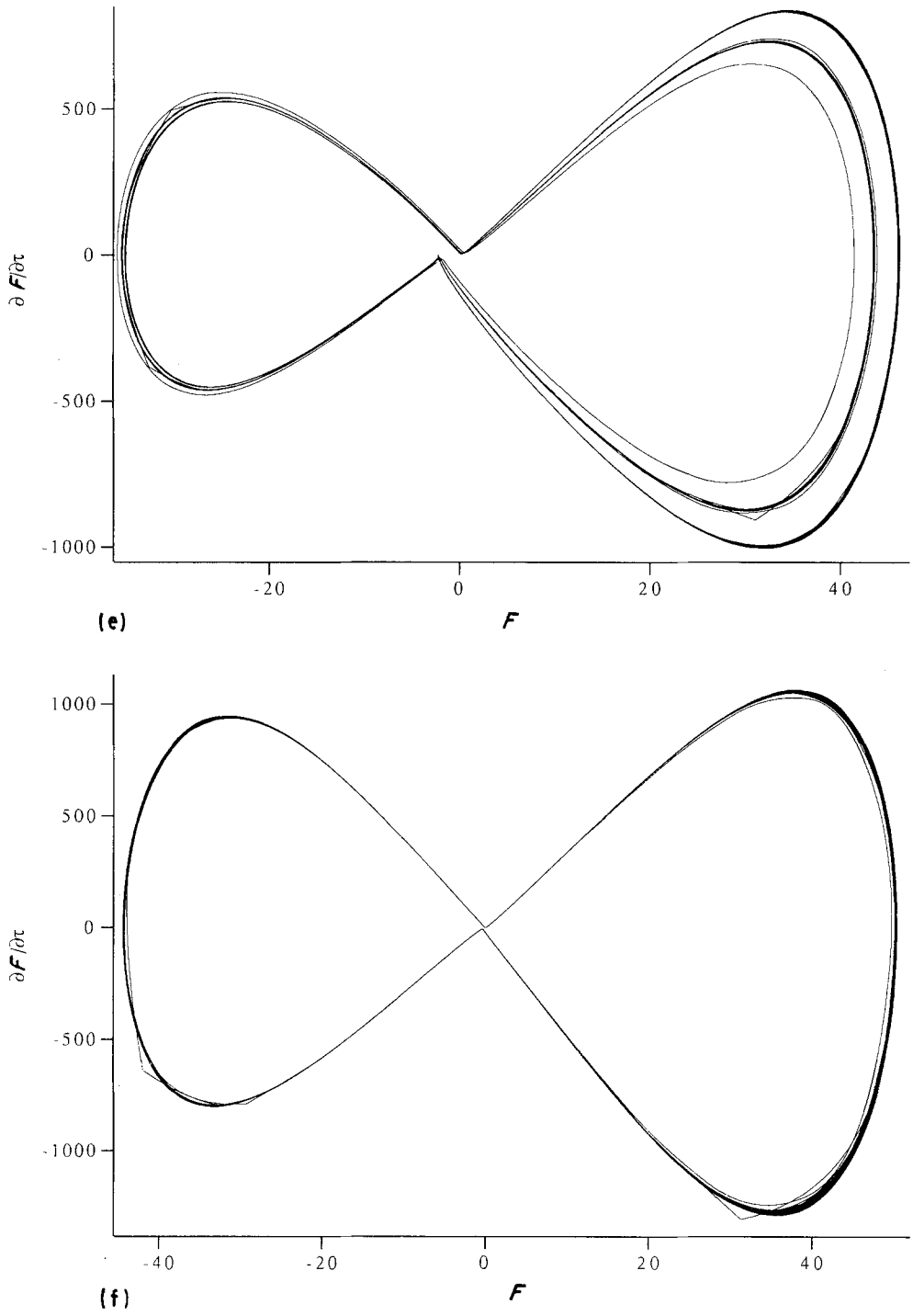

Figure 6 Continued

3.2. Numerical simulations

The primary purpose in developing this model was to determine if aperiodic motions were possible in glass flows, over what range of temperature and geometry these situations would persist, and what types of dynamic behaviour were possible. The information gleaned from the model, in combination with experiments may yield a better understanding of how to control processing conditions.

The set of Equations 12–14 has nine steady-state solutions. Each of these solutions is a function of the cell geometry, the thermophysical properties of the fluid and the temperature difference between the upper and lower surfaces. The solutions are not only a function of the viscosity, but are a function of exactly where on the viscosity–temperature curve one lies. A full analysis of the model equations and their dynamic behaviour is under way, but the breadth of such an analysis is beyond the scope of this paper.

The simulations shown here used the definition for the mean temperature shown in Equation 20 because the results for the critical Rayleigh number calculated using this definition exhibited better qualitative correspondence with experimental data than did those based on Equation 19. The starting point for the integration of the differential equations was chosen arbitrarily as $F = 0$; $D = 0.5$; $E = 0$, and was the same for all runs.

Fig. 6a–h show the results of the numerical simulation displayed as phase-plane diagrams. At low

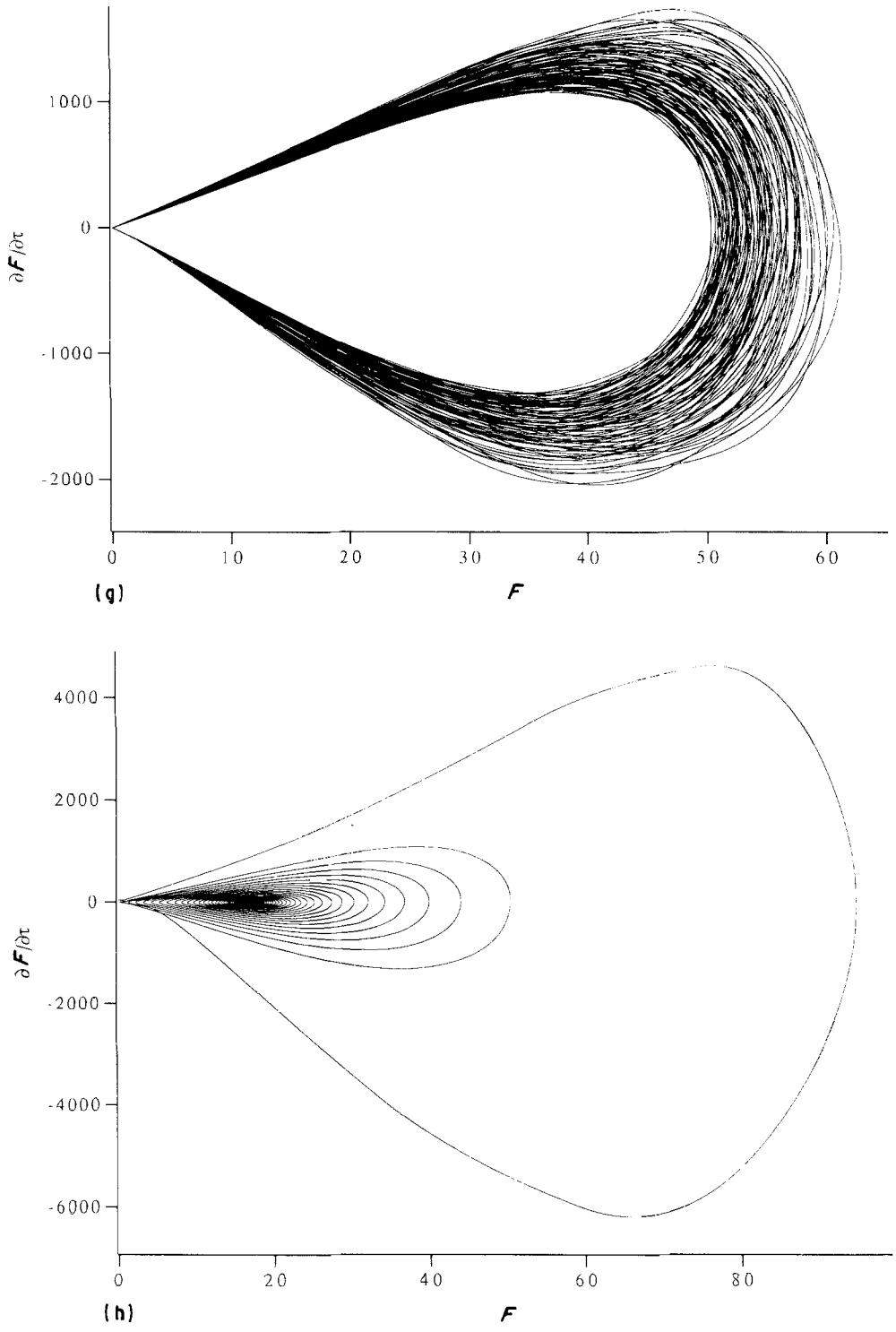

Figure 6 Continued

Rayleigh numbers, steady convective solutions are stable. At a critical point, steady convection becomes unstable and aperiodic motions take over. Despite the fact that there are nine steady-state solutions, the simulation shows that only three are dominant with one being the unstable conductive solution at the origin. Aperiodic flow remains the preferred dynamic situation over a wide range of Rayleigh numbers. As the temperature difference between surfaces is increased (by lowering the temperature of the upper surface), the viscosity of the upper layers become great enough to affect flow in the lower layer. The aperiodic flow becomes damped and decays through a series of bifurcations to states which resemble limit-cycles of different periods (Fig. 6d–h). Here, the non-linear terms in the flow Equation 12 become the dominant components of the solution and finally, force the overall flow back into a steady convective pattern again. As the temperature difference, ΔT, is increased, the horizontal and vertical temperature gradients increase non-linearly making it very difficult to control the properties of the glass (Fig. 7a–f). Once steady flow is favoured, at the highest ΔT investigated, the steady-state temperature gradient is high, but never as high as the highest gradients observed when aperiodic flow is evident.

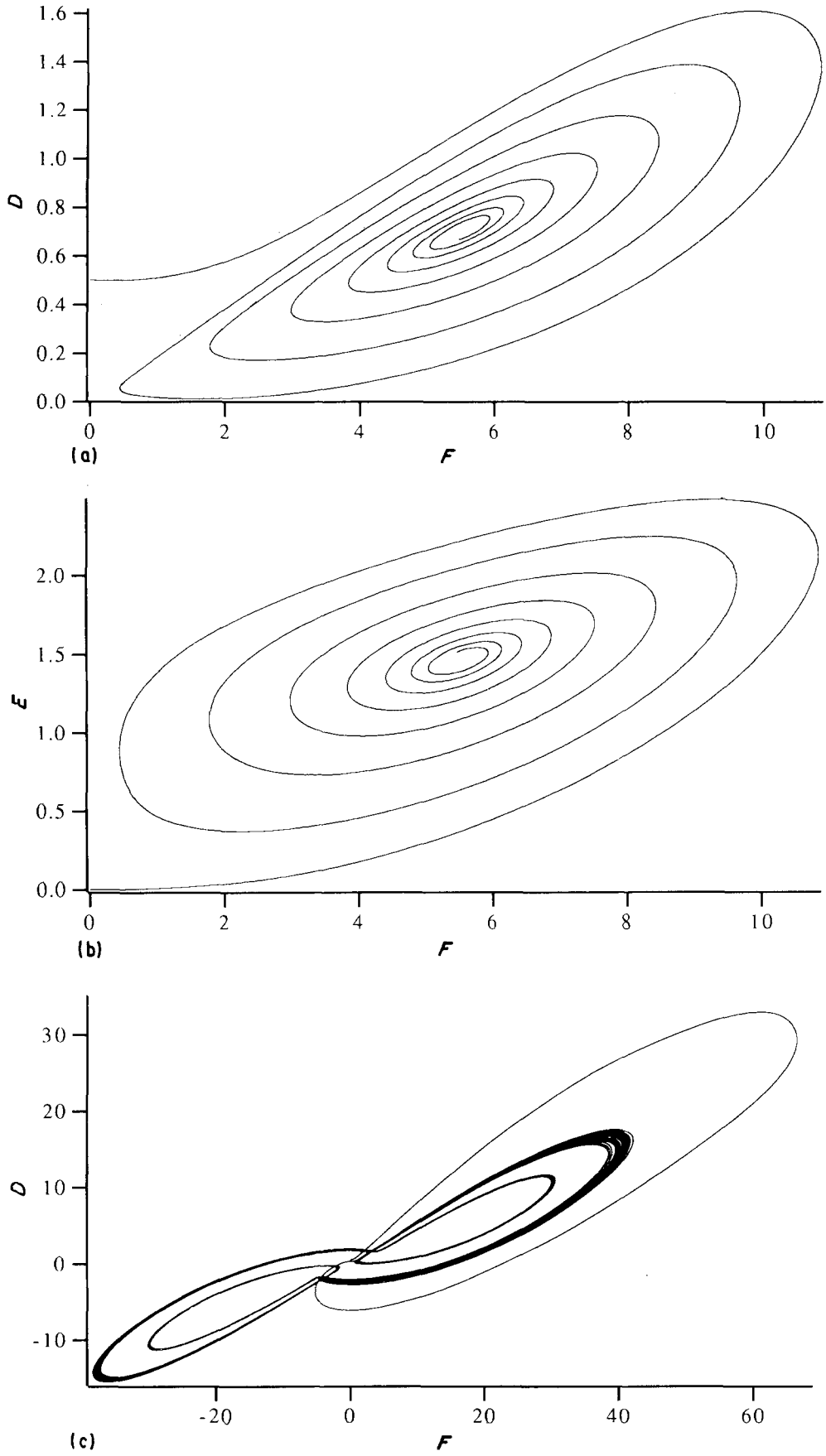

Figure 7 Non-linear temperature gradients in the horizontal (F–D) and vertical (F–E) directions: (a, b) $r = 12.5$, $Pr = 10.5$, $\Delta T = 5\,^{\circ}C$, $a^2 = 0.5$; (c, d) $r = 141.2$, $Pr = 20.5$, $\Delta T = 110\,^{\circ}C$, $a^2 = 0.5$; (e, f) $r = 182.6$, $Pr = 23.1$, $\Delta T = 160\,^{\circ}C$, $a^2 = 0.5$.

The analytical results at small ΔT show that the flow model approximates reality in that limit. The numerical simulation results presented in Fig. 6 show that the model also approximates reality at high ΔT. The high ΔT result corresponds to a quenching solution where if one were to increase ΔT still further, one would expect the solution to continue to decay toward the conductive limit where $F = D = E = 0$ is the only

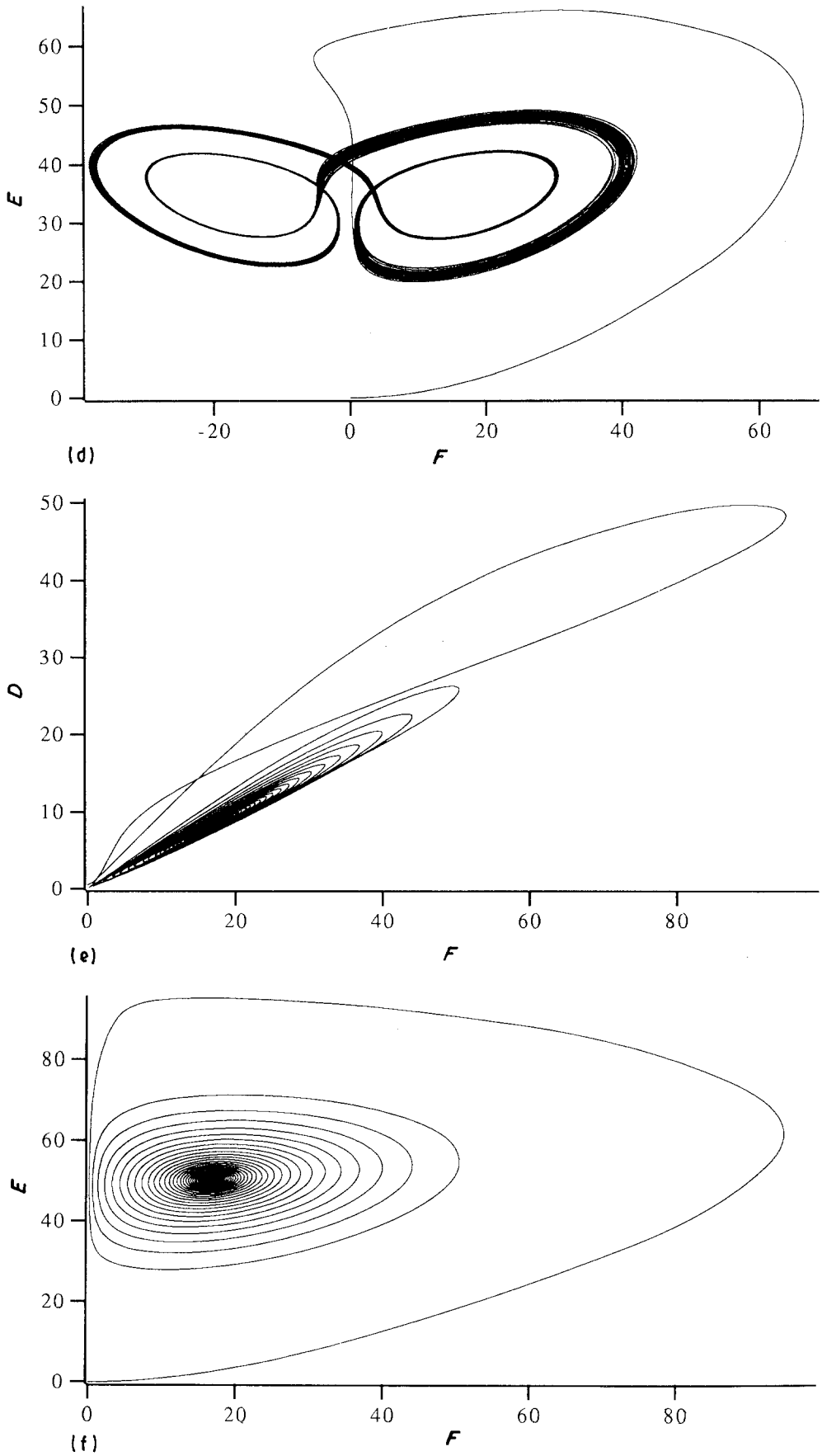

Figure 7 Continued

stable state. The progression from totally aperiodic flow to aperiodic with strong periodicities superimposed makes intuitive sense, since one would expect the flow to decay from a chaotic state to a steady flow state through some type of periodic regime. The simulation here shows only one possible dynamic sequence. The full spectrum of solutions will be the subject of a future paper.

The results of the model simulations have implications for glass processing in general and photosensitive glass processing in particular. In instances where a glass is not well mixed in the furnace or where cord is to be avoided in thick glass samples, one would want to control the surface temperatures during processing to ensure that the glass is held for a time in the region of aperiodic flow where excellent mixing would occur. The model results indicate that the aperiodic regime is fairly broad so that very tight temperature control is not required. In processing a photosensitive glass, one would want to remain at either of the two extremes presented in Fig. 6. Here, to aid in controlling the oxidation state in the glass, one would want to ensure that the flow and temperature fields were well damped so that strong, aperiodic gradients would not occur.

4. Conclusions

A glass–ceramic material was developed to act as a flow visualization material. Preliminary experiments with this material indicate that aperiodic, thermally induced, convective flows can be sustained under normal processing conditions. These flows and the stress and temperature gradients induced are most likely responsible for the anomalous behaviour seen in these materials, and for the difficulties encountered in their development and in their production on industrial and experimental scales.

A simple model describing the dynamics of variable-viscosity fluids was developed and was shown to be in qualitative agreement with more sophisticated models as well as with experimental results. The model was shown to simulate the dependence of the critical Rayleigh number for the onset of convection on the viscous properties of the fluid at low ΔT and also simulate quenching behaviour when the temperature differences were high. The primary features of the model were the predictions of:

(a) steady convective flow at low ΔT, $0 < \Delta T \leqslant 7.5\,^{\circ}\mathrm{C}$

(b) aperiodic flow at moderate ΔT, $7.5 \leqslant \Delta T \leqslant 90\,^{\circ}\mathrm{C}$

(c) strong periodicities superimposed on aperiodic flow, $90 \leqslant \Delta T \leqslant 155\,^{\circ}\mathrm{C}$

(d) steady flow at high ΔT, $160\,^{\circ}\mathrm{C} \leqslant \Delta T$

References

1. S. D. STOOKEY, G. H. BEALL and J. E. PEARSON, *J. Appl. Phys.* **49** (1978) 5114.
2. J. R. BOOKER, *J. Fluid Mech.* **76** (1976) 741.
3. H. HAUCKE and R. ECKE, *Physica* **25D** (1987) 307.
4. C. Q. HOARD, C. R. ROBERTSON and A. ACRIVOS, *Int. J. Heat Mass Transf.* **13** (1970) 849.
5. J. MAURER and A. LIBCHABER, *J. Phys. Lett. Paris* **41** (1980) L515.
6. F. M. RICHTER, *J. Fluid Mech.* **89** (1978) 553.
7. E. F. C. SOMERSCALES and T. S. DOUGHERTY, *ibid.* **42** (1970) 755.
8. D. B. WHITE, *ibid.* **191** (1988) 247.
9. F. H. BUSSE, *J. Math. Phys.* **46** (1967) 140.
10. *Idem, J. Fluid Mech.* **30** (1967) 625.
11. F. H. BUSSE and H. FRICK, *ibid.* **150** (1985) 451.
12. F. H. BUSSE and J. A. WHITEHEAD, *ibid.* **47** (1971) 305.
13. C. CERISIER, C. JAMOND, J. PANTOLINI and C. PEREZGARCIA, *Phys. Fluids* **30** (1987) 954.
14. S. CHANDRASEKHAR, "Hydrodynamic and Hydromagnetic Stability" (Dover Publications, New York, 1961) Chs 1 and 2.
15. A. CLOOT and G. LEBON, *J. Fluid Mech.* **145** (1984) 447.
16. J. H. CURRY, J. R. HERRING, J. LONCARIC and S. A. ORSZAG, *ibid.* **147** (1984) 1.
17. T. M. EIDSON, *ibid.* **158** (1985) 245.
18. M. GOLUBITSKY, J. W. SWIFT and E. KNOBLICH, *Physica* **10D** (1984) 249.
19. D. R. JENKINS and M. R. E. PROCTOR, *J. Fluid Mech.* **139** (1984) 461.
20. O. JENSSEN, *Acta Polytech. Scand.* **24** (1963) 1.
21. R. KESSLER, *J. Fluid Mech.* **174** (1987) 357.
22. S. F. LIANG, PhD thesis, Stanford University (1969).
23. E. N. LORENZ, *J. Atmos. Sci.* **20** (1963) 130.
24. *Idem, Tellus* **12** (1960) 243.
25. W. V. R. MALKUS and G. VERONIS, *J. Fluid Mech.* **4** (1958) 225.
26. D. S. OLIVER and J. R. BOOKER, *Geophys. Astrophys. Fluid Dynam.* **27** (1983) 73.
27. E. PALM, *J. Fluid Mech.* **8** (1960) 183.
28. F. M. RICHTER, H. C. NATAF and S. F. DALEY, *ibid.* **129** (1983) 173.
29. B. SALTZMAN, *J. Atmos. Sci.* **19** (1962) 329.
30. K. C. STENGEL, D. S. OLIVER and J. R. BOOKER, *J. Fluid Mech.* **120** (1982) 411.
31. P. D. SWANSON and J. M. OTTINO, *ibid.* **213** (1990) 227.
32. C. TAYLOR and A. Z. IJAM, *Computer Meth. Appl. Mech. Engng* **19** (1979) 429.
33. K. E. TORRANCE and D. L. TURCOTTE, *J. Fluid Mech.* **47** (1971) 113.
34. F. WRAY, PhD thesis, University of Cambridge (1978).
35. A. P. BOSS, *Rev. Geophys. Space Phys.* **21** (1983) 1511.
36. W. R. JACOBY and H. SCHMELING, *Phys. Earth Planet. Interiors* **29** (1982) 305.
37. D. P. McKENZIE, J. M. ROBERTS and N. O. WEISS, *J. Fluid Mech.* **62** (1974) 465.
38. E. R. OXBURGH and D. L. TURCOTTE, *Rep. Prog. Phys.* **41** (1978) 1249.
39. F. M. RICHTER, *J. Geophys. Res.* **84** (1979) 6783.
40. H. SCHMELING and W. R. JACOBY, *J. Geophys.* **50** (1981) 89.
41. H. SCHMELING, *J. Geophys. Res.* **94** (1989) 12463.
42. D. L. TURCOTTE and E. R. OXBURGH, *Ann. Rev. Fluid Mech.* **4** (1972) 33.
43. D. L. TURCOTTE and G. SCHUBERT, "Geodynamics–Applications of Continuum Physics to Geological Problems" (Wiley, New York, 1982).
44. W. R. JACOBY, *Teçtonophysics* **35** (1976) 103.
45. C. KINCAID and P. OLSON, *J. Geophys. Res.* **92** (1987) 13832.
46. J. S. TURNER, *Earth Planet. Lett.* **17** (1973) 369.
47. L. SHARTSIS, S. SPINNER and W. CAPPS, *J. Amer. Ceram. Soc.* **35** (1952) 155.

Received 16 January
and accepted 2 August 1991